

Computer-modelled deformation mechanism maps for hot uniaxially pressed Bi-2223 superconductor

M. P. JAMES, B. A. GLOWACKI

Interdisciplinary Research Centre in Superconductivity, University of Cambridge, Cambridge CB3 0HE, and Department of Materials Science and Metallurgy, University of Cambridge, Cambridge CB2 3QZ, UK

A. TAMPIERI, G. CELOTTI

Research Institute for Ceramics Technology - CNR, Via Granarolo, 64-48018 Faenza (RA), Italy

A deformation mechanism map represents the densification behaviour of a green powder body. A map is created by evaluating the rate-equations for five types of densification mechanisms: yield, boundary diffusion, volume diffusion, power-law creep, and Nabarro–Herring creep. These rates are summed where appropriate and integrated to give the density at a given pressure, temperature and time; this can then be plotted on a map. Such maps have been created for hot-pressed Bi-2223, using the HIP 6.0 computer software. Four temperature–density deformation maps were created at different pressing pressures and for two types of powder: a solid-state reacted powder and a pyrolysed organic precursor powder. The resulting maps are compared and discussed in relation to a set of experimental results.

1. Introduction

The low critical current in bulk superconductors, especially in strong magnetic fields, is the main limitation to be overcome before they can be utilized in major applications such as superconducting magnetic shielding and current leads. The two major causes of the low J_c behaviour in bulk polycrystalline Bi-2223 superconductors are weak links at the grain boundaries [1], and flux line movements within the grains arising from severe flux creep [2].

Across most high-angle grain boundaries, the flow of transport current is severely limited, especially in the presence of a magnetic field. Grain-boundary weak links are not clearly understood; however, disturbed crystal structure, chemical deviation, the presence of secondary non-superconducting phases, the presence of microcracks and anisotropy of the electronic properties at high-angle boundaries of the crystals, can all contribute to low values of critical current of the intergrain region, and thus of the ceramic as a whole. It is well known that high density and a high degree of grain alignment improve the weak links between grains [3].

Hot pressing has been used to increase the density of bulk Bi-2223 samples [4], and also to increase the texture by increasing grain alignment [5, 6], both of which increase critical current values. Hot pressing increases density by increasing the stresses present at the particle contacts, adding plastic yielding and

power-law creep to the pressureless diffusional densification mechanisms.

The modelling of densification and the development of rate equations for the different mechanisms has been described in the literature [7]. The modelling of densification and the mechanisms by which different powders undergo densification at different temperatures, pressures and for different periods of time can provide information to simplify the optimization of the many hot-pressing process variables. This information may be presented in the form of a deformation mechanism map [8]. A deformation mechanism map is a graphical representation of the rate equations for the diffusional densification mechanisms, such as boundary diffusion and volume diffusion, together with the rate equations for power-law creep and Nabarro–Herring creep and the equation for yield. The contributions to the densification rate from each of the mechanisms is evaluated and, as they are independent, the rates are summed to give the total densification rate. This is then integrated to get the density at a given pressure, temperature, and time. The density can then be plotted against either pressure or temperature, often with time contours. Such a map has been used to predict the densification of $\text{YBa}_2\text{Cu}_3\text{O}_{7-z}$ [9]. To enable deformation maps to be constructed accurately and efficiently, the HIP 6.0 program has been written [10] to aid in the construction of the maps.

The densification of a green powder body is related to the time, temperature, and pressure of consolidation. Of paramount importance are the material properties of the powder, these describe the mechanical and transport characteristics and the geometry of the powder. The largest uncertainty in the accuracy of a deformation map lies with the material properties entered into the equations. Where possible a temperature coefficient is used to correct properties, such as modulus, for the temperature of densification. The first step in the construction of a map is to collate the required data which are used to compute a map. These are then refined using data from experimental observations.

2. Experimental procedure

A density–pressure deformation mechanism map was constructed at room temperature to model the cold pressing of solid-state powder. Density–temperature deformation mechanism maps were constructed using the HIP 6.0 software for three different fixed pressures; 7, 11 and 15 MPa.

A summary of the required material data used in conjunction with the HIP 6.0 program, and an explanation as to the origin of the values, are given below. The solid density has been found, by hot pressing samples to 100% density, to be approximately $6550.00 \text{ kg m}^{-3}$ [11]. The melting point of all solids in the powders used was found from DTA analysis to be approximately 1233 K (960 °C). Young's modulus at room temperature has been reported at 64 GPa, using an ultrasonic pulse transmission technique [12].

Yield stress of single Bi-2223 grains at room temperature was calculated using the results of the deformation map constructed at room temperature which modelled the cold uniaxial pressing of solid-state powder. The relative density after yield, Δ_{yield} , is described in Equation 1

$$\Delta_{\text{yield}} = \left[\frac{(1 - \Delta_0)P}{1.3\sigma_y} + \Delta_0^3 \right]^{1/3} \quad (1)$$

Plastic yielding is instantaneous and therefore time is not present in Equation 1. Δ_{yield} is the starting density for the time-dependent mechanisms, σ_y is the yield strength of the particles (MPa). A correct fit to the data on the map was made when the single adjustable parameter, yield strength, was equal to 700 MPa. This value agrees well with literature values [13]. From the material data, the temperature dependence of yield was estimated by the HIP 6.0 software to equal approximately 0.50 [10].

From experimental observation reported in the literature, the power-law creep exponent has been calculated at 3.80 [14]. The reference stress for power-law creep is a characterization of creep, and is the stress (MPa) required to cause a steady tensile creep rate of 10^{-6} s^{-1} at a temperature of one-half the absolute melting temperature. This value was calculated by the HIP 6.0 program from the temperature, tensile stress, and observed strain rate in a conventional creep test, and gave a value of approximately 7 TPa [10]. The activation energies for power-law

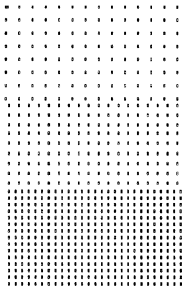
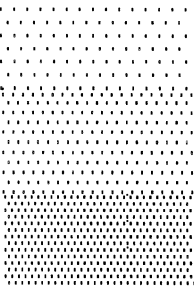
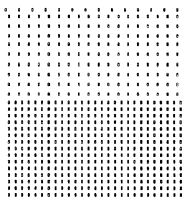
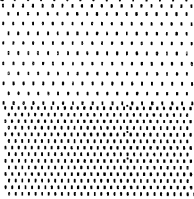
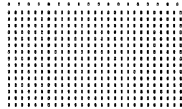

creep have been given as $520 \pm 50 \text{ kJ mol}^{-1}$ for Bi-2201, $630 \pm 210 \text{ kJ mol}^{-1}$ for Bi-2212, and $960 \pm 210 \text{ kJ mol}^{-1}$ for Bi-2223 [14]. As this property has large error bars, it was used to tune the deformation map; the final value used was 660 kJ mol^{-1} .

Owing to the layered nature of these compounds, diffusion parallel to the *c*-axis is a difficult process and there is a large anisotropy between the diffusion coefficient parallel to *c*, D_c , and the diffusion coefficient for the *ab* plane, D_{ab} [15]. Because D_{ab} is far greater than D_c , the diffusion coefficient for polycrystalline material, D_{poly} , approximately equals D_{ab} . As the structure of the *ab* planes for the three bismuth compounds is the same, the diffusion in the *ab* plane of all three superconductors will be the same. Therefore, D_{poly} will be the same for all three superconductors. Bi-2223 has five different atomic components contributing to the chemical formula, all with different atomic radii and valance, and different diffusion rates, different activation energies, and different diffusion anisotropy is, i.e. D_{ab}/D_c , although in all cases $D_{ab} \gg D_c$. The most relevant diffusion coefficient is that for the slowest-diffusing atom, it being the rate-limiting mechanism in diffusion processes.

At the surface of a phase, an atom moving from one site to another is not constrained by having to squeeze between surrounding atoms on all sides. Therefore, atomic mobility is greater on the surface and takes place with a lower activation energy. Likewise the less-dense packing of atoms at a grain boundary or dislocation leads to greater atomic mobility than in the crystal lattice and a lower activation energy than that for volume diffusion. Therefore, diffusion coefficients are required for each of these mechanisms. The volume diffusion coefficient, D_v , refers to any diffusion process within the bulk or volume of the crystal. The surface diffusion coefficient, D_s , measures diffusion along a surface. The boundary diffusion coefficient, D_b , measures diffusion along an interface or boundary, including grain boundaries and dislocations. A general rule for diffusion in crystalline oxides applies, that activation energy for surface diffusion is approximately half that of volume diffusion, and the activation energy for boundary and dislocation diffusion lies between volume diffusion and surface diffusion [16].

Experiments have been reported on the bismuth compounds [17, 18], the combined results of which suggest that strontium is the slowest-diffusing atomic species. There was no systematic variation of D_v of strontium with the number of Cu–O layers in the bismuth compounds, i.e. between Bi-2201, Bi-2212 and Bi-2223. The pre-exponential for volume diffusion was calculated as $6 \times 10^{13} \text{ m}^2 \text{ s}^{-1}$ from an activation energy for volume diffusion of 580 kJ mol^{-1} , and volume diffusion coefficient for Bi-2223 at 800 °C in oxygen of $3.8 \times 10^{-12} \text{ cm}^2 \text{ s}^{-1}$ [17]. No boundary diffusion or surface diffusion data have been published for Bi-2223 or any other HTS, so the general rule described above was applied. These values were also adjusted when the deformation maps were tuned, giving an activation energy for boundary diffusion of 435 kJ mol^{-1} , a pre-exponential for boundary diffu-

TABLE I Density of shading indicating the extent of grain growth

Pore separation	Grain growth factor	Pore dragging
	1.1	
	2	
	5	

sion of $0.60 \text{ m}^3 \text{ s}^{-1}$, an activation energy for surface diffusion of 290 kJ mol^{-1} , and a pre-exponential for surface diffusion of $6 \times 10^{10} \text{ m}^3 \text{ s}^{-1}$.

The weighted atom-volume for a compound is the volume transported when one atom of the slower-diffusing species moves; as strontium has been found to be the slowest-diffusing species for the bismuth series of superconductors, the atom volume is half the molecular volume of Bi-2223, thus is equal to $5.40 \times 10^{-28} \text{ m}^3 \text{ atom}^{-1}$.

The resulting maps are divided into fields by heavy solid lines. These fields show the range of dominance for a given mechanism. The abbreviations used for the mechanisms are: YIELD is yield, V-DIFF1 and VDIFF2 are volume diffusion stage 1 and stage 2, respectively, B-DIFF1 is boundary diffusion stage 1, PL-CRP1 and PL-CRP2 are power law creep stage 1 and stage 2, respectively. When a deformation mechanism map has a field where a time-dependent mechanism is dominant, the map will then have time contours in the form of a series of lines. The far right-hand line is the lowest time line in the series, usually 1 h, and the time increases by a factor of two as the series moves to the left, i.e. 1, 2, 4, and 8 h lines.

The style of shading indicates whether grain growth occurs by the migrating grain boundaries dragging pores along (pore dragging), or pulling away from the pores (pore separation). The grain-growth factor is the factor by which the final grain size is larger than the original particle size. The density of shading indicates the extent of grain growth, according to the scheme shown in Table I.

A selection of experimental data was collected to tune the deformation maps and compare differences between powder preparation methods and powder compositions. Two powder preparation methods were used in the hot-pressing experiments. This gave two different powder particle sizes and different grain sizes within the particles. The range of particle size was measured by the maximum commonly occurring radius divided by the mean radius and is known as the ratio of radii. The powders formed via a solid-state reaction, denoted as S1, S2 and S3, starting from oxides and carbonates [19], gave a particle radius of $8 \mu\text{m}$ with a grain diameter of $2 \mu\text{m}$ within the particle. The ratio of radii was equal to 2. The powder formed via an organic precursor, denoted P1, using the pyrolysis technique [20], gave a particle radius of $4 \mu\text{m}$

TABLE II The four powders used for the experimental data set

Powder	Preparation method	Composition
S1	Solid state	$\text{Bi}_{1.84}(\text{Pb})_{0.34}\text{Sr}_{1.91}\text{Ca}_{2.03}\text{Cu}_{3.06}$
S2	Solid state	$\text{Bi}_{1.8}(\text{Pb})_{0.35}\text{Sr}_{1.9}\text{Ca}_{2.1}\text{Cu}_3$
S3	Solid state	$\text{Bi}_{1.8}(\text{Pb})_{0.35}\text{Sr}_{2.1}\text{Ca}_{1.9}\text{Cu}_3$
P1	Pyrolysis	$\text{Bi}_{1.8}(\text{Pb})_{0.35}\text{Sr}_{1.9}\text{Ca}_{2.1}\text{Cu}_3$

TABLE III Experiments used for data in the deformation mechanism maps

Powder	Pressure (MPa)	Temperature ($^{\circ}\text{C}$)	Time (h)	Relative density
S1	7.0	790	2	0.920
	7.0	800	2	0.930
	7.0	810	2	0.950
	7.0	820	2	0.970
	7.0	830	2	1.000
	7.0	810	1	0.940
	7.0	810	2	0.950
	7.0	810	3	0.960
	7.0	810	4	0.960
	7.0	810	6	0.970
P1	7.0	790	2	0.925
	11.0	800	2	0.975
S2	15	780	2	0.890
	15	800	2	0.945
	15	820	2	0.988
S3	15	780	2	0.830
	15	800	2	0.900
	15	820	2	0.950

with a grain diameter of $0.5 \mu\text{m}$ within the particle. The ratio of radii was equal to 3. The mean particle size was determined by means of a Sedigraph using ethanol as a solvent.

The morphology of the powder was investigated by scanning electron microscopy (Leica Cambridge Ltd); the powder was suspended in ethanol and sprayed on the sample holder. The melting point of the powder was determined by differential thermal analysis (Polymer Science, UK). Table II shows the four different powder compositions used and the preparation method.

Powder produced by the solid-state method was pressed at 100, 200, 300 and 400 MPa in a steel die at room temperature. The density of the green powder bodies were measured and this provided the data for the density–pressure deformation mechanism map. Table III shows the series of data used in the deformation maps. The powders for hot-pressed samples were uniaxially cold pressed into pellets at 14.7 MPa. The initial relative density of the green body was 0.65, and the initial pore pressure was taken as 0.10 MPa. These pellets were then hot pressed in an alumina die using an Instron press. The alumina die and plunger were sputtered with silver to minimize reaction with the superconductor. The heating rate used was $10^{\circ}\text{C min}^{-1}$ and the sintering atmosphere was air. The density measurements were performed using the Archimedes' method.

3. Results and discussion

The deformation mechanism map in Fig. 1 is a density–pressure map. When a powder is cold uniaxially pressed, initial densification occurs via particle rearrangement and fracture; as the density increases, the plastic yielding mechanism contributes to densification. The map clearly shows the pressure required to cold press the powder to a given density.

As plastic yielding is time independent, the map has no time contours. The correct fit to the cold-pressed data on the map was made when the single adjustable parameter, yield strength, was equal to 700 MPa. However, the yield strength calculated via microhardness measurements for the sintered ceramic body formed from the solid-state powder was 300 MPa [21]; the yield strength of a polycrystalline body is heavily dependent on microstructure. The appropriate yield strength entered as the material property for the construction of the deformation mechanism map is higher, because the yield strength required is that of the grains of the powder, not the final ceramic body. The equation for yield, shown earlier, is independent of particle size, so the map is appropriate for all particle sizes. The map in Fig. 2 is a density–temperature deformation map, with a set pressure of 7 MPa, for the solid-state powder S1. The S1 data set can be broken into two parts; increasing temperature with constant time, and increasing time with constant temperature. The increasing temperature with constant time data, 790–830 °C in 10 °C steps at 2 h, shows good correlation to the second theoretical time contour in Fig. 2, and this is the 2 h contour. The increasing time, 1, 2, 3, 4 and 6 h, at 810 °C set of data, follows the increasing theoretical time contours, 1, 2, 4 and 8 h, fairly closely. The dominant deformation mechanism at 7 MPa is volume diffusion.

The pyrolysis powder P1 was used for the data in Fig. 3. The particle size, grain size and ratio of radii have been changed whilst keeping other experimental and material properties constant. As particle size and grain size are reduced, boundary diffusion plays an increasingly dominant role in the early stages of densification. The smaller grains have moved the time contours to a lower temperature by approximately 10 °C.

The pattern of grain growth has also changed with the powder morphology. Initial grain growth occurred with pore dragging for both the solid-state powder and the pyrolysis powder. However, unlike the solid-state powder, at the final stages of densification the pyrolysis powder undergoes grain growth with grain-boundary separation, rather than pore dragging. Any inclusions dragged along the grain boundary during grain growth, such as pores, increase in size and their mobility decreases. The increase in the ratio of radii and the decrease in grain size of the pyrolysis powder, increases the driving force for grain growth, enabling the grain boundaries to separate from the less-mobile pores.

Using the same powder, P1, the pressure is increased to 11 MPa in Fig. 4. The power-law creep mechanism field grows; although it is not the dominant densification mechanism, it does contribute to

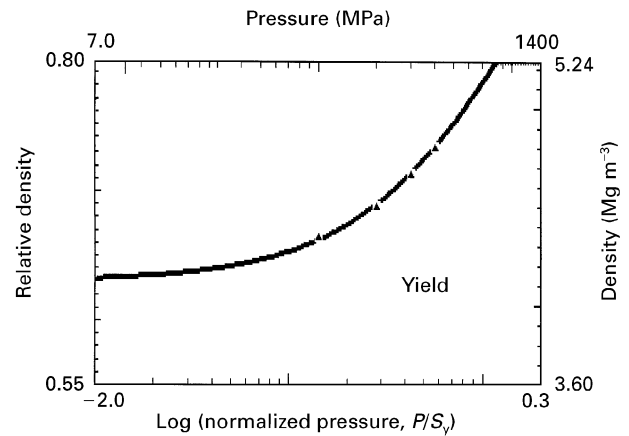


Figure 1 Density–pressure deformation mechanism map for the cold uniaxial pressing of solid-state powder at 25 °C. $a = 0.008$ mm, $\Delta_0 = 0.63$, $p_i = 0.01$ MPa.

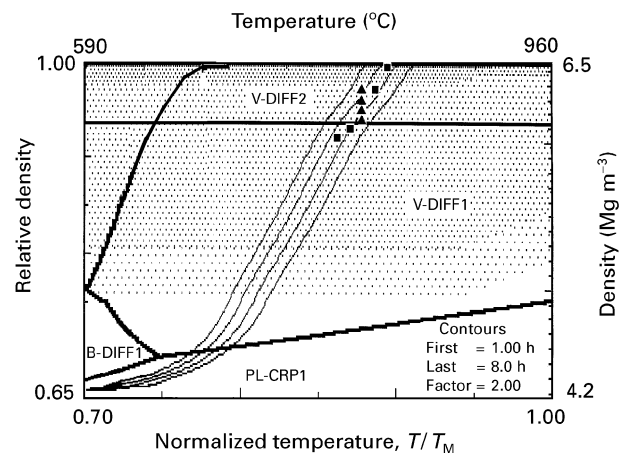


Figure 2 Density–temperature deformation mechanism map for powder S1 at 7 MPa. (■) Increasing T with constant time, (▲) increasing time with constant T . $a = 0.008$ mm, $\Delta_0 = 0.65$, $p_i = 0.10$ MPa.

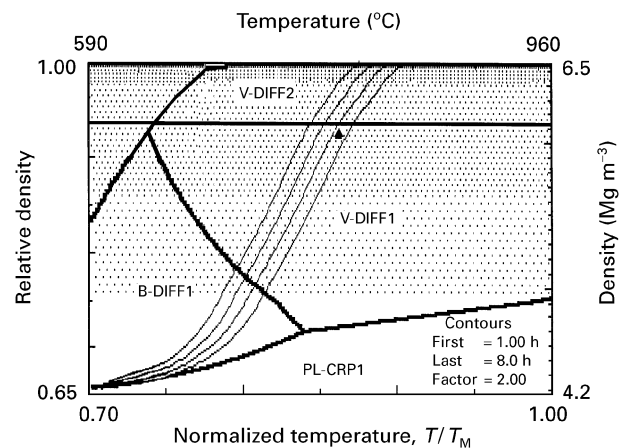


Figure 3 Density–temperature deformation mechanism map for powder P1 at 7 MPa. $a = 0.004$ mm, $\Delta_0 = 0.65$, $p_i = 0.10$ MPa.

the densification and to the texturing of the sample. The data and theoretical time contours continue to correlate well. As expected, an increase in the pressure has enabled the time contours to move to a slightly lower temperature compared to those in Fig. 3. In

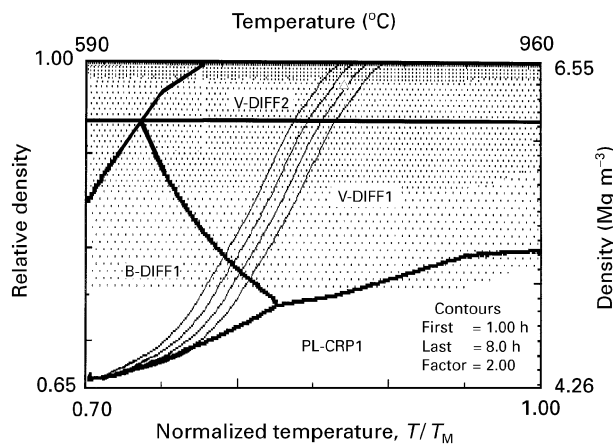


Figure 4 Density-temperature deformation mechanism map for powder P1 at 11 MPa. $a = 0.004$ mm, $\Delta_0 = 0.65$, $p_i = 0.01$ MPa.

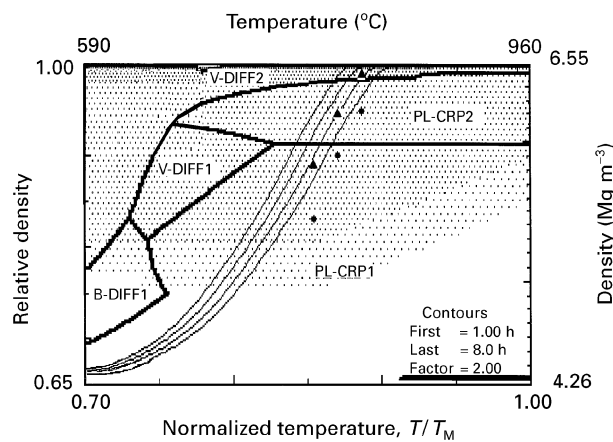


Figure 5 Density-temperature deformation mechanism map for powders (▲) S2 and (*) S3 at 15 MPa. $a = 0.008$ mm, $\Delta_0 = 0.65$, $p_i = 0.10$ MPa.

combination with a 10°C rise in sintering temperature, the sample density has risen from 0.925 to 0.975 relative density.

The deformation map in Fig. 5 shows the solid-state powders S2 and S3 at 15 MPa. The S2 powder has a strontium to calcium ratio of 1.9:2.1, whilst the S3 powder has a strontium to calcium ratio of 2.1:1.9, i.e. strontium rich. Although the samples have been treated at the same temperature and pressure for the same period of time, the strontium-rich samples are, on average, 5% less dense than the respective S2 samples.

This is due to the well-known sluggishness of reaction kinetics in samples with strontium-rich compositions [22, 23], and is caused by the refractoriness of SrO and the high decomposition temperature of SrCO_3 . This map has the correct material parameters for the S2 powder, and therefore the S2 data points lie on the correct time contour, 2 h. Again an increase in the pressure has enabled the time contours to move to a slightly lower temperature compared to those in Fig. 2.

4. Conclusion

Deformation mechanism maps have been created for hot-pressed Bi-2223 using the HIP 6.0 computer soft-

ware. The cold uniaxial pressing of Bi-2223 powder produced via solid-state reaction was modelled using a pressure-density deformation mechanism map with the temperature set to 25°C . The correct fit of the cold-pressed data to the map gave a yield strength for the powder grains of 700 MPa. Four temperature-density deformation maps were created for 7, 11 and 15 MPa using two types of powder: solid-state reacted and pyrolysed organic precursor produced via pyrolysis. An increase in pressure and temperature increased the density for a given pressing time, as did the reduction in grain and particle size between the two different types of powder. The different powder morphologies also affected the theoretical grain growth characteristics shown on the maps. The accuracy of a deformation-mechanism map is limited by the data and equations used to create it. However, the data showed good correlation to the theoretical time contours on the maps and they provide very useful information with which to plan experiments and analyse results.

References

1. D. DIMOS, P. CHAUDHARI, J. MANNHART and F. K. LEGOUES, *Phys. Rev. Lett.* **61** (1988) 219.
2. V. M. VINOKOR, P. H. KES and A. E. KOSHELEV, *Phys. C* **168** (1990) 29.
3. S. JIN and J. E. GRAEBNER, *Mater. Sci. Engng* **B7** (1990) 243.
4. A. TAMPIERI and G. N. BABINI, *Jpn J. Appl. Phys. Lett.* **30** (1991) 1163.
5. J. G. NOUDEM, J. BEILLE, D. BOURGAULT, A. SUIPICE and R. TOURNIER, *Phys. C* **230** (1994) 42.
6. N. CHEN, A. C. BIONDO, S. E. DORRIS, K. C. GORETTA, M. T. LANAGAN, C. A. YOUNGDAHL and R. B. POEPEL, *Supercond. Sci. Technol.* **6** (1993) 674.
7. A. S. HELLE, K. E. EASTERLING and M. F. ASHBY, *Acta Metall.* **26** (1985) 2163.
8. H. J. FROST and M. F. ASHBY, "Deformation-Mechanism Maps" (Pergamon Press, Oxford, UK, 1982).
9. A. M. CAMPBELL, P. P. EDWARDS, R. JONES, A. D. HIBBS, M. F. ASHBY, J. E. EVETTS and B. GLOWACKI, in "Proceedings of the European Workshop on High T_c Superconductors and Potential Application", Fiera del mare, Genova, Italy, 1-3 July 1987, eds J. Vilain and S. Gregoli, (Commission of European Communities, Brussels, 1987) p. 61.
10. M. F. ASHBY, HIP 6.0: Software for constructing maps for sintering and hot isostatic pressing", Cambridge University Engineering Department (1990).
11. H. IKEDA, R. YOSHIKAWA, K. YOSHIKAWA and N. TOMITA, *Jpn J. Appl. Phys. Lett.* **29** (1990) 430.
12. M. MURALIDHAR, K. NANDA KISHORE, Y. V. RAMANA and V. HARI BABU, *Mater. Sci. Engng* **B13** (1992) 215.
13. J. DOMINEC, P. VASEK, P. SWOBODA, V. PLECHACEK and C. LAERMANS, *Mod. Phys. Lett.* **B7** (1992) 1049.
14. K. C. GORETTA, E. J. ZAMIROWSKI, J. M. CALDERON-MORENO, D. J. MILLER, N. CHEN and T. G. HOLESIINGER, *J. Mater. Res.* **9** (1994) 541.
15. J. L. ROUTBORT and S. J. ROTHMAN, *J. Appl. Phys.* **76** (1994) 5615.
16. W. D. KINGERY, H. K. BOWEN and D. R. UHLMANN, "Introduction to ceramics", (Wiley, New York, 1976) Chs 6, 14.
17. N. CHEN, S. J. ROTHMAN and J. L. ROUTBORT, *J. Mater. Res.* **8** (1993) 2465.
18. M. V. SLINKINA, L. I. VOLOSENTSEVA, G. I. DONTSOV, A. S. ZHUKOVSKAYA and A. A. FOTIEV, *Superconductivity* **5** (1992) 1819.

19. G. CELOTTI, A. TAMPIERI, R. MASINI and M. C. MALPEZZI, *Phys C* **225** (1994) 346.
20. A. TAMPIERI, G. CELOTTI, F. RICCIADIELLO and G. RUSSO, *ibid.* **227** (1994) 300.
21. A. TAMPIERI, G. CELOTTI, S. GUICCIARDI and C. MELANDRI, *Mater. Chem. Phys.* **42** (1995) 188.
22. B. HONG, J. HAHN and T. O. MASON, *J. Amer. Ceram. Soc.* **73** (1990) 1965.
23. D. C. SINCLAIR, J. T. S. IRVINE and A. R. WEST, *J. Mater. Chem.* **2** (1992) 579.

*Received 30 May
and accepted 17 September 1996*